Supporting Information

Electrochemical CO_2 Reduction in the Presence of SO_2 Impurities on a Nitrogen-doped Carbon Electrocatalyst

Shilong Fu[a,d], Bowen Sha[b,d], Asvin Sajeev[a,d], Ming Li[a,c,d], Thijs J.H. Vlugt[b,d], Othonas A. Moultos[b,d], Wiebren de Jong[a,d], Ruud Kortlever[a,d,*]

[a] *Large-Scale Energy Storage, Process & Energy Department, Faculty of Mechanical Engineering, Delft University of Technology, Leeghwaterstraat 39, 2628 CB Delft, The Netherlands*

[b] *Engineering Thermodynamics, Process & Energy Department, Faculty of Mechanical Engineering, Delft University of Technology, Leeghwaterstraat 39, 2628 CB Delft, The Netherlands*

[c] *Product and Process Engineering, Chemical Engineering Department, Faculty of Applied Sciences, Delft University of Technology, Van der Maasweg 9, 2628 HZ Delft, The Netherlands*

[d] *e-Refinery Institute, Delft University of Technology, Leeghwaterstraat 39, 2628 CB Delft, The Netherlands*

Corresponding Author

*Dr. Ruud Kortlever Email: r.kortlever@tudelft.nl

Table of Contents

Computational Methods

All density functional theory calculations were performed using Gaussian 09 Rev B.01 software on the DelftBlue supercomputer at TU Delft.[1] The hybrid PBE0 functional was employed with the def2-SVP basis set for geometry optimization and frequency analysis, while the def2-TZVPP basis set was used for higher-accuracy electronic energy calculations.[2–4] A cluster model approach was adopted, with peripheral atoms of silver and carbon materials frozen during optimization.[5,6] The selected basis sets automatically incorporated Stuttgart small-core pseudopotentials for silver atoms, effectively reducing the number of explicit electrons in calculations while accounting for scalar relativistic effects at negligible computational cost.[7] Convergence of self-consistent field (SCF) iterations was assisted using a 0.5 Hartree energy level shift. Dispersion interactions were treated with Grimme's DFT-D3 method (Becke-Johnson damping version) for improved accuracy.[8] Thermal corrections were computed via Shermo 2.6 software, applying Grimme's quasi-rigid rotor harmonic oscillator (QRRHO) treatment to low-frequency vibrational modes.[9,10]

Post-processing analyses including independent gradient model based on Hirshfeld partition (IGMH) and density of states (DOS) calculations were conducted using Multiwfn 3.8(dev).[11–13] Structural visualization and rendering utilized Visual Molecular Dynamics (VMD) 1.9.3.[14] The thermodynamic corrections include zero-point energy (ZPE) and temperature-dependent contributions to thermodynamic properties. For instance, the correction to Gibbs free energy follows the expression:

$$G_{corr} = ZPE + \Delta G_{0\text{-}298K}$$

For each species, the Gibbs free energy was obtained by summing the high-accuracy electronic energy (computed with Gaussian 09) and the thermodynamic corrections (calculated using Shermo), expressed as:

$$G = E_{ele} + G_{corr}$$

For surface-SO_2 interactions, where no electron or proton transfer is involved, the adsorption energy was calculated directly as:

$$\Delta G_{ad} = G_{surface+SO2} - G_{surface} - G_{SO2}$$

For *SOOH, the situation is more complex. Following Nørskov's methodology,[15] we consider the influence of external voltages and proton transfer effects through the following approach:

$$\Delta G_{ad} = G_{surface+SOOH} - G_{surface} - G_{SO2} - 1/2G_{H2} + eU - 2.23\ kT*pH$$

Experimental Section

Chemicals and materials

All chemical were used as received without further purification. Electrolytes and 1 M HCl solutions were prepared from ultrapure water (Milli-Q IQ 7000, 18.2 MΩ·cm). Urea (CN_2H_4O, 99%), sodium hydroxide (NaOH, 98%), potassium bicarbonate ($KHCO_3$, 99.95%) and Nafion perfluorinated resin solution (5 wt.% in lower aliphatic alcohols and 15-20% water) were purchased from Sigma-Aldrich. Hydrochloric acid (HCl, 37%), and isopropanol (C_3H_8O, 99%) were obtained from VWR International. Carbon paper (Toray, TGP-H-60) was purchased from Thermo Scientific Chemicals, while the silver foil (25 × 25 × 1 mm, 99.995%) and the platinum foil (25 × 25 × 0.1 mm, 99.99%) were purchased from

MaTeck GmbH. The carbon gas diffusion layer (GDL, Sigracet 39BB) and platinized titanium screen were purchased from Fuel Cell Store. Silver nanoparticles (Ag NP, 99.9%, 20 – 40 nm) were purchased from Thermo Scientific Chemicals. Iridium oxide nanoparticles (IrO_2 NP, 99.99%) were purchased from Alfa Aesar.

Catalyst preparation

The activated nitrogen-doped biochar (ANBC) catalyst was synthesized using a one-step pyrolysis method.[16] In brief, the received sugarcane bagasse (Maharashtra, India) was thoroughly washed three times with ultrapure water to eliminate any dust and gravel impurities from the raw materials and then dried in an oven at 105 °C overnight. Once dried, the sugarcane bagasse was finely ground and sieved to obtain particle sizes of smaller than 425 µm before use. Subsequently, 5 g of sugarcane bagasse powder, 10 g of urea, and 15 g of sodium hydroxide (NaOH) were combined in a crucible in a mass ratio of 1:2:3. The mixture was stirred for 30 minutes to ensure homogeneity before being transferred to a muffle furnace. The furnace was heated to 800 °C at a ramping rate of 10 °C/min under a N_2 atmosphere (100 sccm, 99.99%, Linde Gas), where it was held for 1 h. After naturally cooling down to the ambient temperature, the obtained product was washed with 1 M HCl at 60 °C for 4 hours to eliminate sodium-containing salts and other impurities. Afterwards, the product was rinsed and filtered thoroughly with ultrapure water until the washing effluent reached a neutral pH. Finally, the resulting black powder was collected and dried at 105 °C for 12 h and the obtained catalyst was designated as activated N-doped biochar (ANBC).

Characterization

The morphology of the ANBC powder was visualized using a JEOL JSM-6500F scanning electron microscope (SEM) operating at an acceleration voltage of 15 kV, equipped with an energy-dispersive X-ray spectroscopy (EDX) detector (Ultradry, Thermo Scientific). The microstructure of ANBC was further investigated by transmission electron microscopy (TEM) with a JEOL JEM1400 microscope operated at 120 kV. TEM specimens were prepared by mixing the ANBC sample with isopropanol, followed by ultrasonic dispersion for 15 minutes. The resulting suspension was then deposited onto a copper TEM grid coated with a lacey carbon film. The specific surface area and porosity of ANBC were characterized by isothermal N_2 adsorption-desorption at 77 K, using a Micromeritics TriStar II 3020 instrument. The sample was degassed at 300 °C for 15 h before measurement. The specific surface area (S_{BET}) of ANBC was calculated using the Brunauer-Emmett-Teller (BET) equation, while the pore size distribution plot was obtained by applying the Density Functional Theory (DFT) method. The surface area (S_{micro}) and volume (V_{micro}) of micropores were assessed by the t-plot method. The total pore volume (V_{Total}) was calculated by single-point adsorption total pore volume analysis. The crystal structure of the ANBC was performed using an X-ray diffractometer (Bruker AXS D2 Phaser) with Cu-Kα radiation (λ = 0.15406 nm). The scanning 2θ angle range was set between 10.0° and 80.0° with a step length of 0.020°. Raman spectrum of ANBC was recorded from 500 to 3000 cm^{-1} on a LabRAM HR Evolution microscope (Horiba Scientific) with an excitation wavelength of 514 nm. The surface chemical compositions of ANBC were investigated by X-ray photoelectron spectroscopy (XPS) using a Thermo Scientific K-Alpha system with an Al Kα X-ray source (1486.6 eV). The C 1s peak position at 284.8

eV was used as an internal standard. CasaXPS (Version 2.3.22PR1.0) was used for the further elemental identification and peak deconvolution.

Additionally, SEM and XPS analyses were conducted on both the drop-cast ANBC electrodes and silver foil electrodes before and after electrolysis to characterize any morphological and compositional changes in the electrodes. All measurements were executed under the same conditions as previously described.

Electrode preparation

The working electrodes for H-cell measurements were prepared using a drop-casting method. 4 mg of ANBC powder was dispersed in a solvent mixture containing 950 µL isopropanol and 50 µL of 5 wt.% Nafion perfluorinated resin solution. The mixture was ultrasonicated for 1 h to obtain a homogeneous ink. Afterwards, 10 µL of the ink was drop casted on a 1 cm^2 round-shaped carbon paper and thoroughly dried at room temperature. The drop-casting procedure was repeated 4 additional times, resulting in a final catalyst loading of approximately 0.2 mg/cm^2. A platinum foil was used as a counter electrode, which was flame annealed at least three times to eliminate any possible impurities before use. A leak-free Ag/AgCl electrode (Innovative instrument, LF-1-45) was used as the reference electrode. The reference electrode was checked before every experiment by comparing with a master Ag/AgCl reference electrode (BASi, MF-2056), which is kept in a pristine working condition and never used for any experiment. The potential drift of the test reference electrode against the master reference electrode was measured by an open circuit potential (OCP) test, ensuring that the drift value remained below 5 mV.

For comparison, a silver foil was also employed as a working electrode. Prior to each measurement, the silver foil was mechanically polished twice with a 1 µm diamond-based suspension (MetaDi supreme, Poly, 1 µm, Buehler) to achieve a mirror-like finish, followed by sonication in isopropanol and ultrapure water to ensure cleanliness.

Electrodes for MEA reactor measurements were fabricated via a spray-coating technique. In a typical procedure, 20 mg of catalyst (ANBC or Ag NPs for the cathode, and IrO_2 NPs for the anode) was dispersed in a mixed solvent comprising 475 µL of isopropanol, 475 µL of deionized water, and 50 µL of a 5 wt.% Nafion solution. Each mixture was sonicated for 1 hour to form a homogeneous catalyst ink.

The ANBC and Ag NP inks were spray-coated onto a preheated carbon gas diffusion layer (2.25 cm × 2.25 cm) maintained at 100 °C, using a handheld airbrush (Conrad HP-101) equipped with a 0.3 mm nozzle and high-purity nitrogen (99.99%, Linde gas) as the carrier gas. Similarly, the IrO_2 dispersion was deposited onto a 3 cm × 3 cm × 0.025 cm platinized titanium mesh. Prior to coating, the titanium mesh was sequentially ultrasonicated in acetone, ethanol, and deionized water to remove surface contaminants. All electrodes were weighed before and after spraying to determine the catalyst loading accurately. The final loadings were 0.2 ± 0.02 mg/cm^2 for the cathode and 1.0 ± 0.1 mg/cm^2 for the anode.

Gas mixer

A gas mixer (Environics® Series 4020) was used to generate the gas mixtures for the electrochemical measurements. The mass flow controllers and gas lines in the gas mixer were coated with SilcoNert® and sealed with Kalrez® to prevent corrosion from SO_2 gas.

Two standard gas cylinders with known concentrations of SO_2 (100 ppm and 10000 ppm, balanced by CO_2, Linde Gas) were used to generate the desired concentrations (100 ppm, 1000 ppm, and 10000 ppm) of SO_2 by diluting with CO_2 (99.999%, Linde Gas). The detailed information about the gas mixtures for electrochemical measurements are listed in Table S2.

Electrochemical measurements

All working electrodes were evaluated in a two-compartment compact H-cell (Figure S8), which was designed by Lobaccaro and co-workers.[17] Each compartment contained 1.8 mL of 0.1 M $KHCO_3$ as the electrolyte and the cathode and anode chambers were separated by an anion exchange membrane (Selemion AMV, AGC Engineering). Before each measurement, the cathodic compartment of the H-cell was purged with pure CO_2 or CO_2 mixed with varying concentrations of SO_2 impurities for 15 minutes to ensure saturation of the catholyte. The pH values of different gas mixtures-saturated electrolytes are listed in Table S3. Electrochemical measurements in this study were conducted using an SP-200 potentiostat (Biologic). All potentials measured in this study were converted to the reversible hydrogen electrode (RHE) scale according to the formula: E (V vs. RHE) = E (V vs. Ag/AgCl) + 0.197 + 0.059 × pH. Linear sweep voltammetry (LSV) measurements were recorded in various gas mixtures-saturated 0.1 M $KHCO_3$ electrolytes at a scan rate of 5 mV/s, spanning potentials from -0.1 to -1.3 V vs. RHE. Chronoamperometric electrolysis measurements were carried out at different applied potentials from -0.7 to -1.3 V vs. RHE and each potential was applied for 1 h. During the chronoamperometry tests, CO_2 or CO_2 mixed with different concentrations of SO_2 impurities were purged

continuously into the catholyte with a flow rate of 10 sccm controlled by a mass flow controller. The faradaic efficiencies (FEs) and current densities for various gas products during the 1-hour experiments were calculated based on average values obtained from the data collected between 42 and 54 minutes. For the 8-hour experiments conducted at -1.0 V vs. RHE, the continuous flow rate was maintained at 10 sccm and the FEs were reported every 20 minutes, utilizing the average values from each interval.

The high current density electrolysis tests were conducted in a membrane electrode assembly (MEA) electrolyzer featuring an active area of 5 cm^2 and a serpentine flow field (Dioxide Materials; titanium anode, 904L stainless steel cathode). The MEA was constructed by sandwiching a 5 cm × 5 cm anion exchange membrane (PiperION, 20 μm thickness) between the as-prepared cathode and anode, followed by securing the assembly with eight bolts tightened to a torque of 2.5 Nm.

Prior to entering the cathode compartment, the reactant gas (CO_2 mixture containing 100 ppm SO_2) was humidified by passing through a humidifier at a flow rate of 20 sccm. The humidifier, filled with 5 mL of Milli-Q water, was pre-saturated for 30 minutes with a CO_2 mixture containing 100 ppm SO_2 before each experiment. The anode compartment was continuously fed with 1 M $KHCO_3$ solution at a flow rate of 5 mL/min using a peristaltic pump. A liquid trap was installed near the gas outlet of the electrolyzer to capture any condensed liquid products or moisture, thereby preventing interference with downstream gas chromatography measurements (Figure S19).

Product detection

An in-line gas chromatograph (Compact GC 4.0, Global Analyzer Solutions), equipped with one flame ionization detector (FID) and two thermal conductivity detectors (TCD), was used to quantify the gaseous products every 2 minutes. The gas chromatograph (GC) was calibrated by using five calibration gas cylinders with different concentrations of 50, 100, 1000, 3000, and 8000 ppm of each gas component (H_2, CO, CH_4 and C_2H_4). The calibration curves of H_2, CO, CH_4, and C_2H_4 are shown in Figure S9. The liquid-phase products were collected at the end of the CO_2RR measurements and quantified using a high-performance liquid chromatograph (HPLC, Agilent 1260 Infinity), which was equipped with two Aminex HPX 87-H columns (Bio-Rad). The column oven was maintained at 60 °C constantly, using a 1 mM H_2SO_4 aqueous solution as eluent with a steady flow of 0.6 mL/min and using a refractive index detector (RID) for the product detection. Ion Chromatography (IC, Thermo Fisher Scientific) equipped with a Dionex IonPac AS14A or a Dionex IonPac AS22 column was applied to identify the existence of various anions, such as formate, sulfite and sulfate.

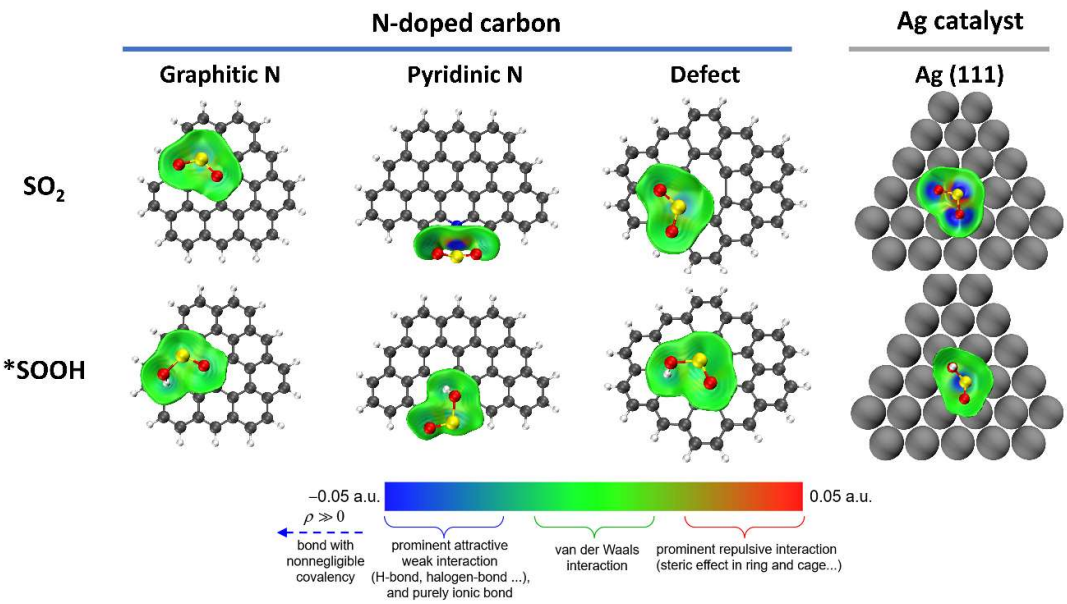

Figure S1. IGMH analysis of the adsorption configurations.

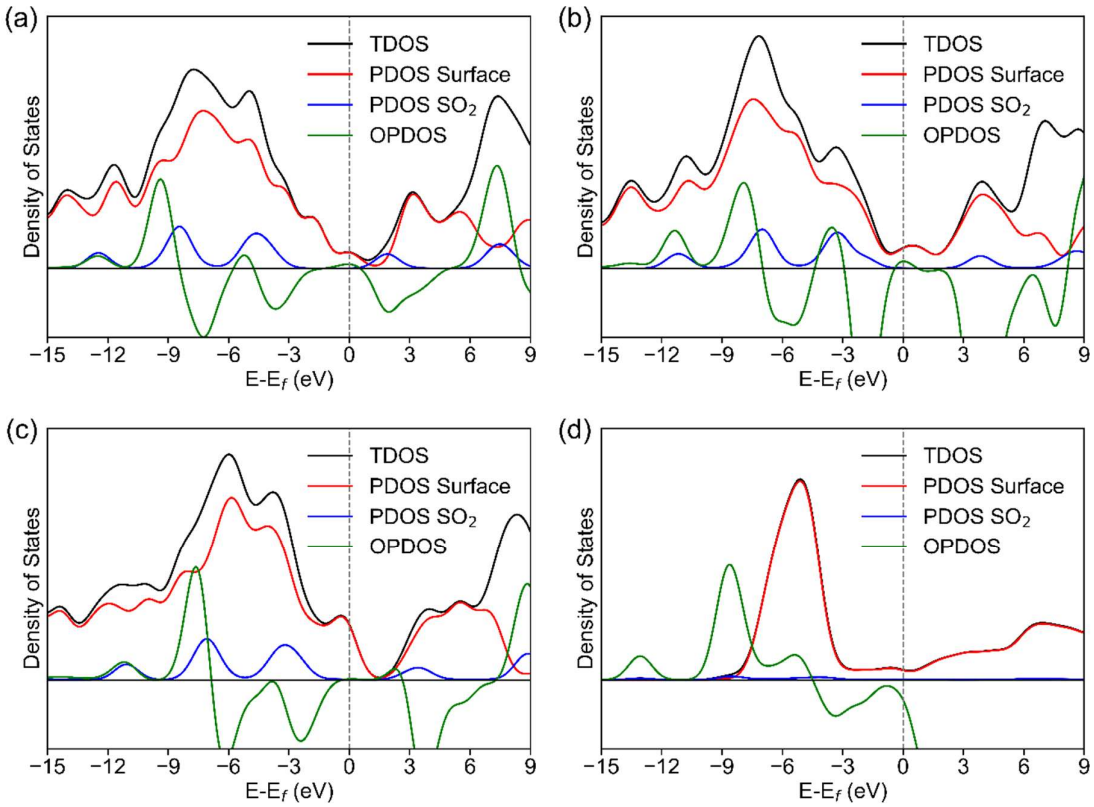

Figure S2. DOS/PDOS/OPDOS for SO_2 adsorbed on (a) graphitic N, (b) pyridinic N, (c) carbon defect, (d) silver (111) surface.

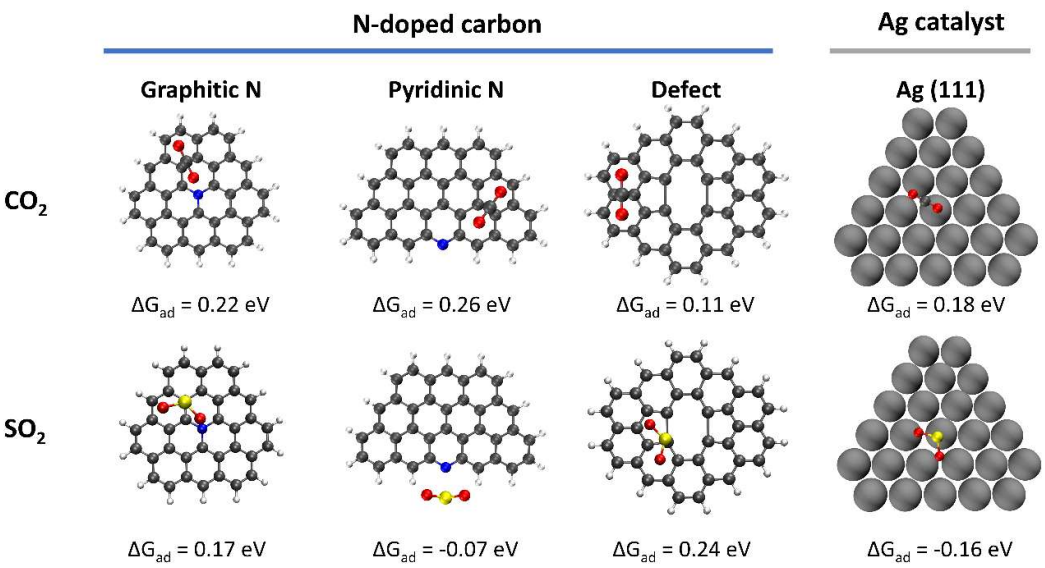

Figure S3. A comparison of CO_2 and SO_2 adsorption modes and ΔG_{ad} adsorption energies on three potential active sites of N-doped carbon catalysts, namely pyridinic nitrogen, graphitic nitrogen and carbon defects, and on the Ag(111) surface.

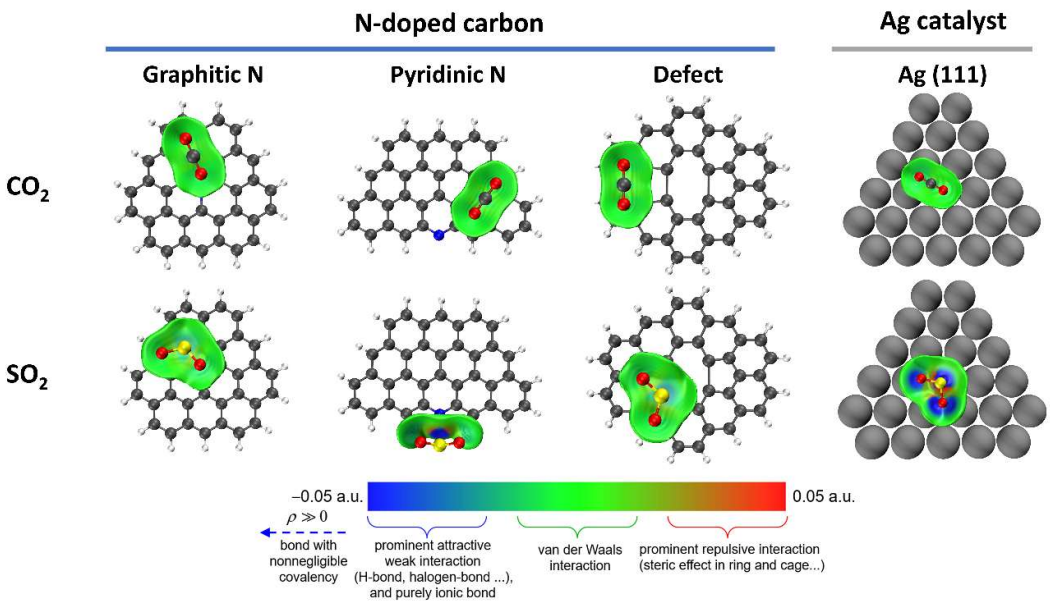

Figure S4. IGMH analysis of the adsorption configurations of CO_2 and SO_2 on N-doped carbon sites, namely pyridinic nitrogen, graphitic nitrogen and carbon defects, and on the Ag(111) surface.

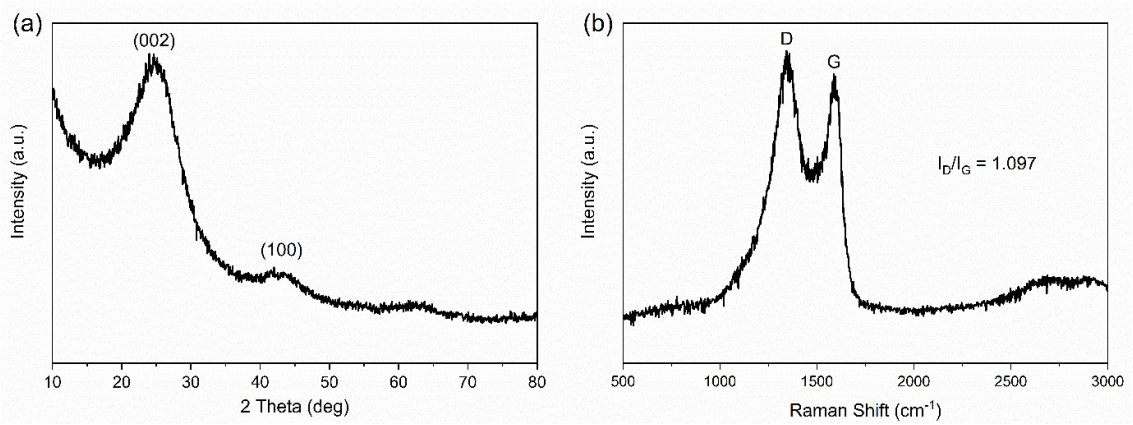

Figure S5. (a) XRD pattern and (b) Raman spectrum of the ANBC catalyst.

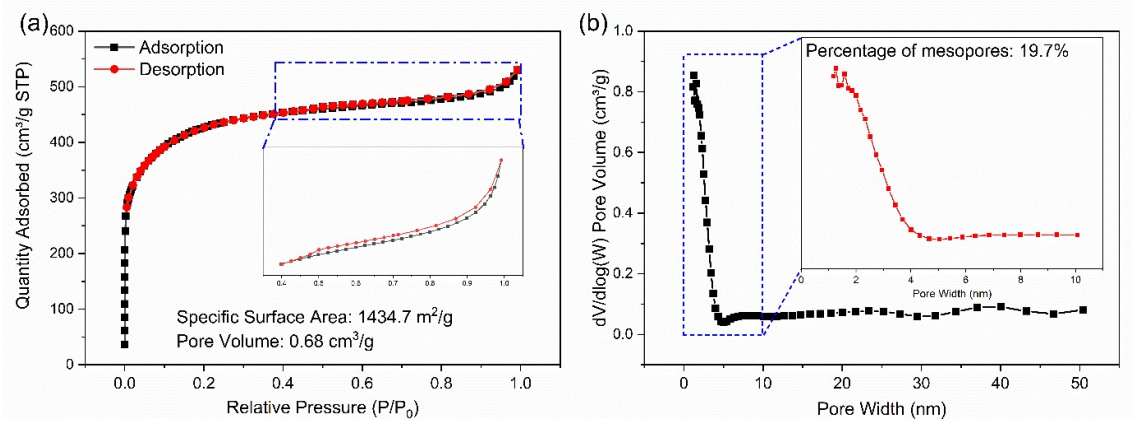

Figure S6. (a) N_2 adsorption-desorption isotherms and (b) Pore size distribution of the ANBC catalyst.

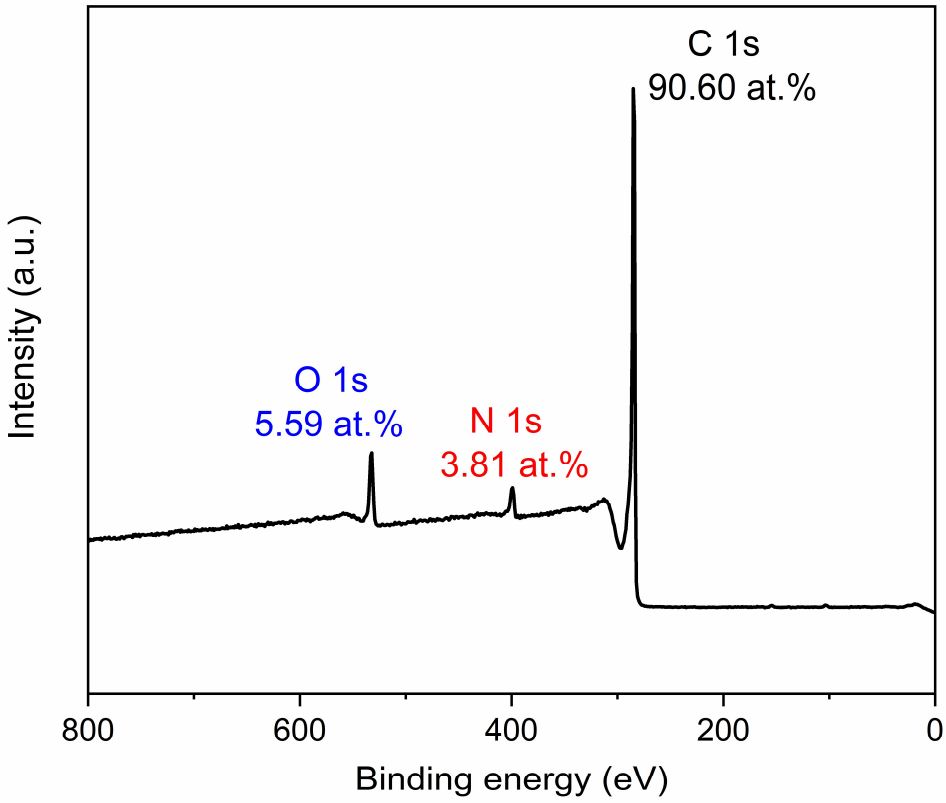

Figure S7. XPS survey spectrum of the ANBC catalyst.

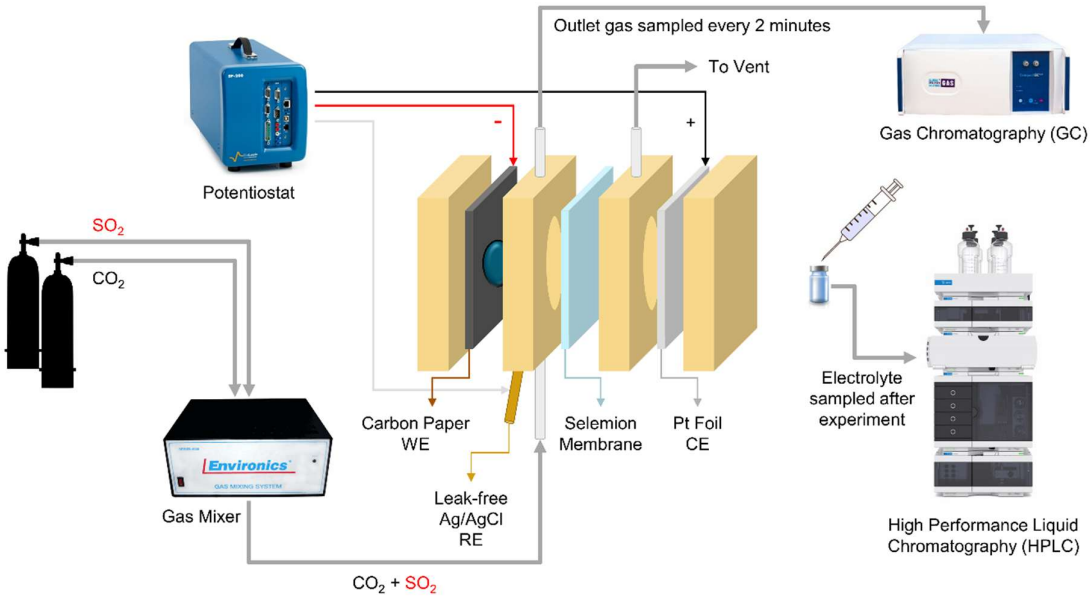

Figure S8. Schematic illustration of the electrochemical measurements system in this study.

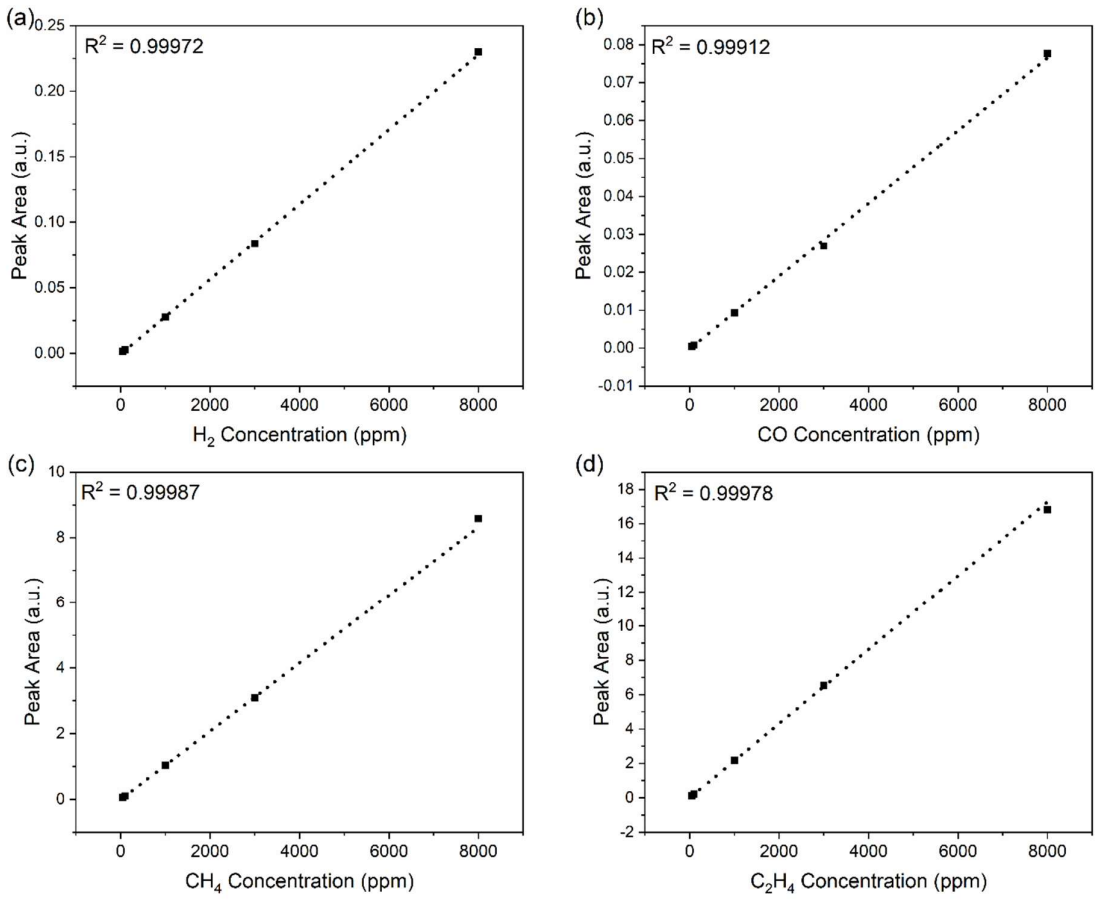

Figure S9. GC calibration curves for (a) H_2, (b) CO, (c) CH_4, (d) C_2H_4.

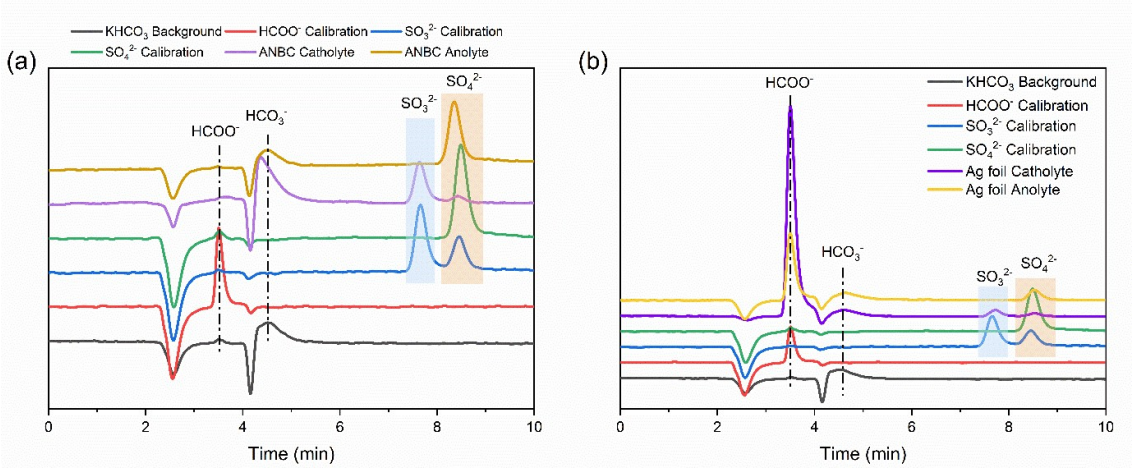

Figure S10. Ion chromatography results of $KHCO_3$ background, as well as formate, sulfite, and sulfate calibration curves. (a) Post-reaction analysis of the catholyte and anolyte from the ANBC electrode after CO_2RR at -1.0 V vs. RHE in the presence of 10000 ppm SO_2. (b) Post-reaction analysis of the catholyte and anolyte from the Ag foil electrode after CO_2RR at -1.0 V vs. RHE in the presence of 10000 ppm SO_2.

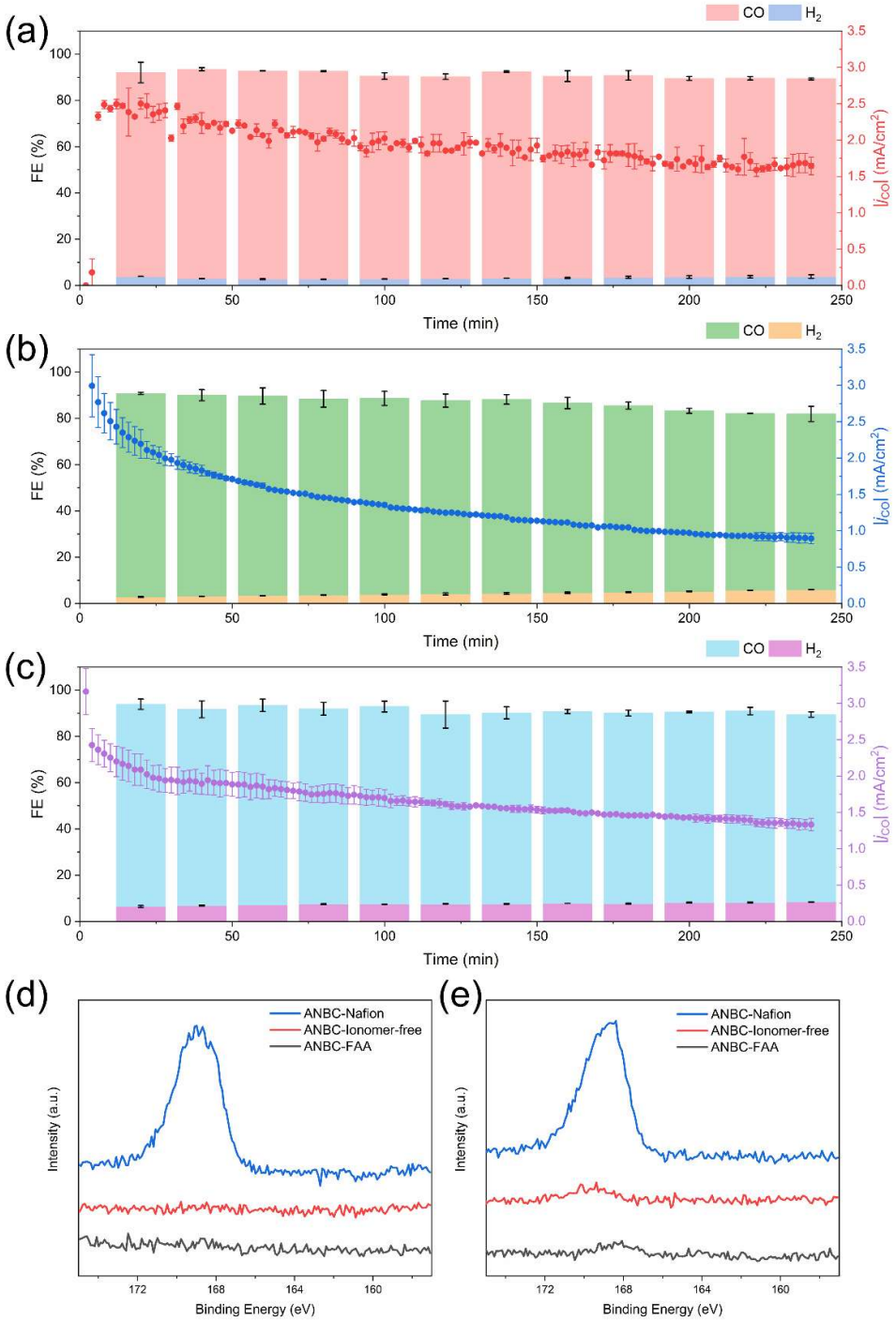

Figure S11. Faradaic efficiencies and j_{CO} during 4-hour tests for (a) Nafion-containing ANBC, (b) Ionomer-free ANBC and (c) FAA-containing ANBC electrodes at -1.0 V vs. RHE in a CO_2 + 100 ppm SO_2 gas mixture saturated 0.1 M $KHCO_3$ electrolyte; and S 2p XPS spectrum of (d) fresh ANBC electrodes and (e) post-reaction ANBC electrodes.

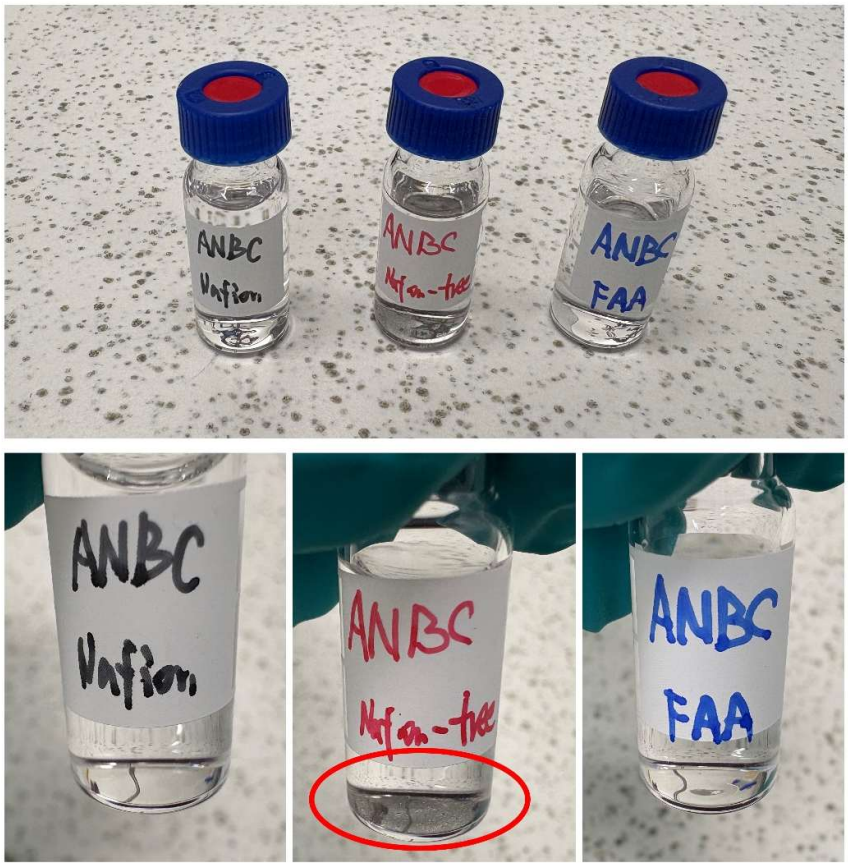

Figure S12. Post-electrolysis catholytes collected from control experiments with different ANBC electrodes.

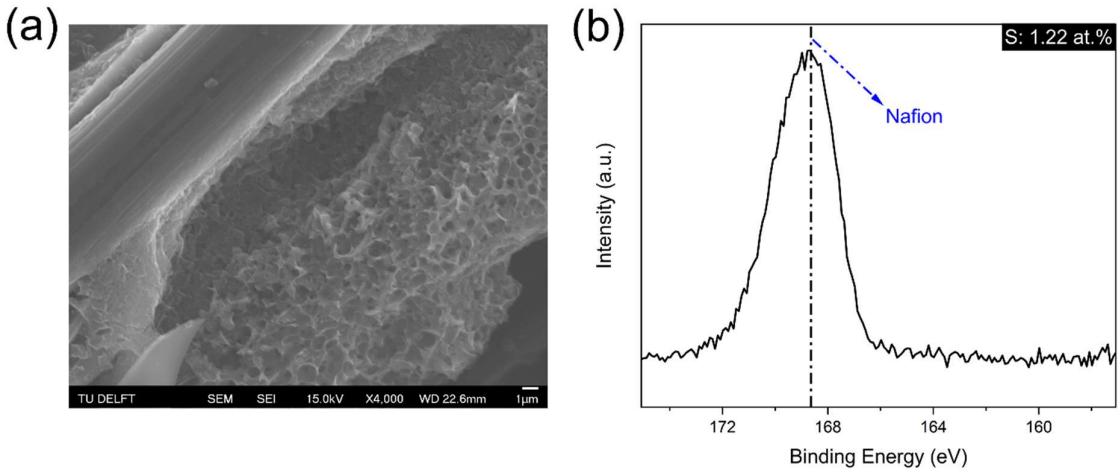

Figure S13. (a) SEM image and (b) S 2p XPS spectrum of fresh ANBC electrode.

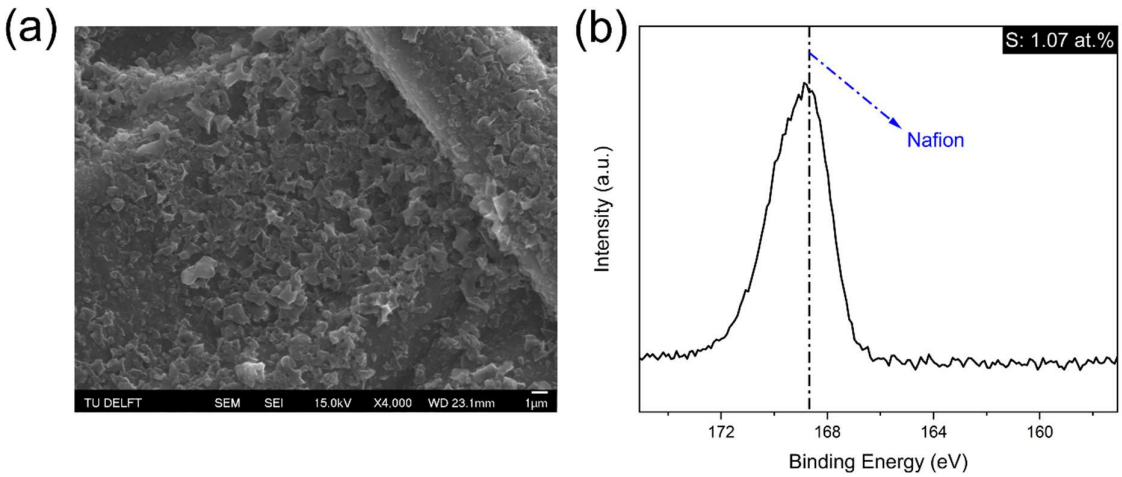

Figure S14. (a) SEM image and (b) S 2p XPS spectrum of ANBC electrode after 8 hours of continuous electrolysis with 100 ppm SO_2 at -1.0 V vs. RHE.

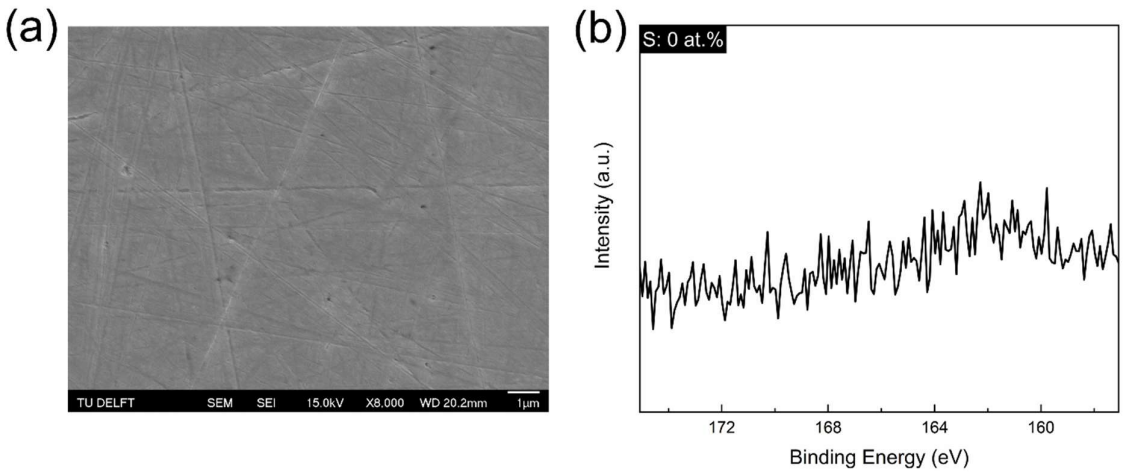

Figure S15. (a) SEM image and (b) S 2p XPS spectrum of fresh Ag foil electrode.

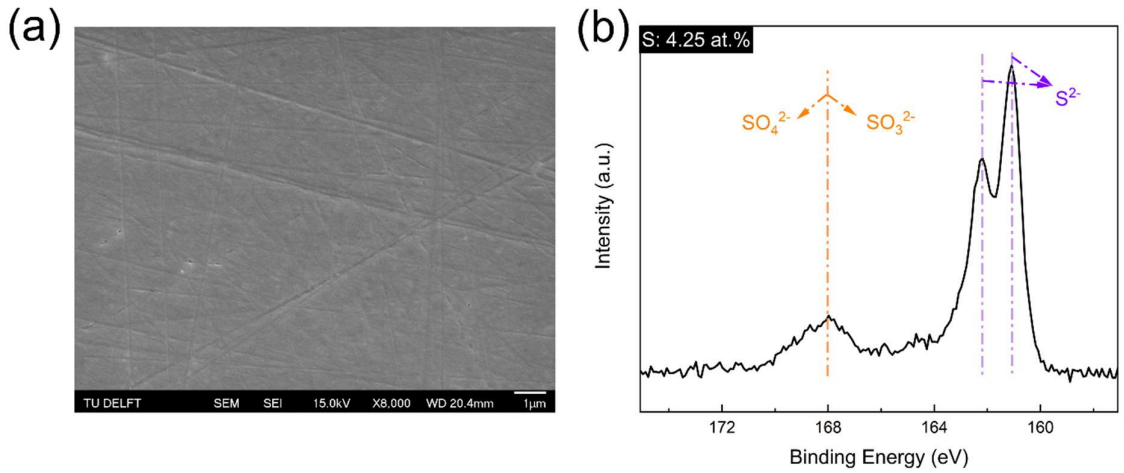

Figure S16. (a) SEM image and (b) S 2p XPS spectrum of Ag foil electrode after 8 hours of continuous electrolysis with 100 ppm SO_2 at -1.0 V vs. RHE.

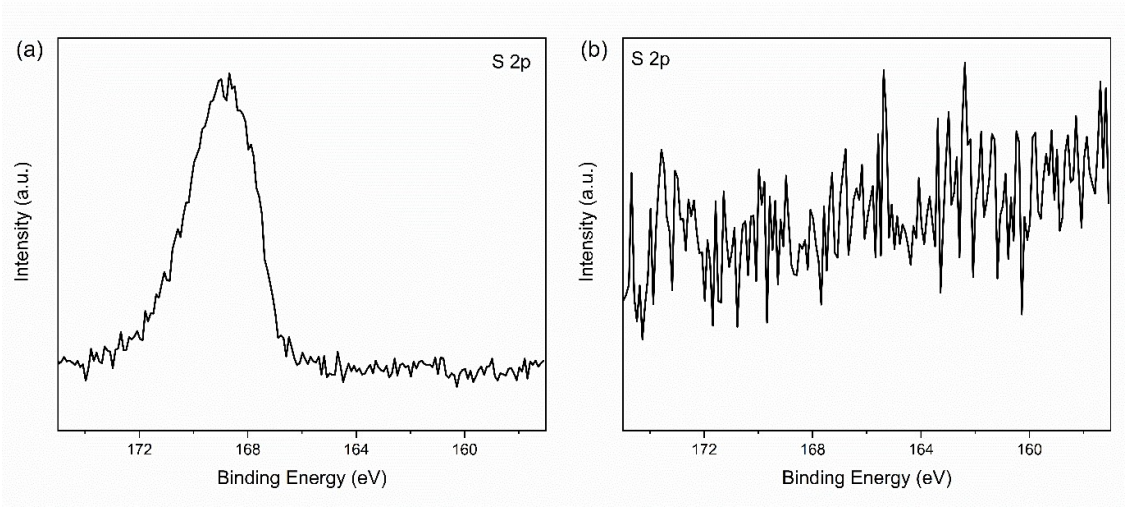

Figure S17. S 2p XPS spectrum of (a)ANBC and (b) Ag foil electrodes after 1 hour open-circuit test with CO_2 + 100 ppm SO_2.

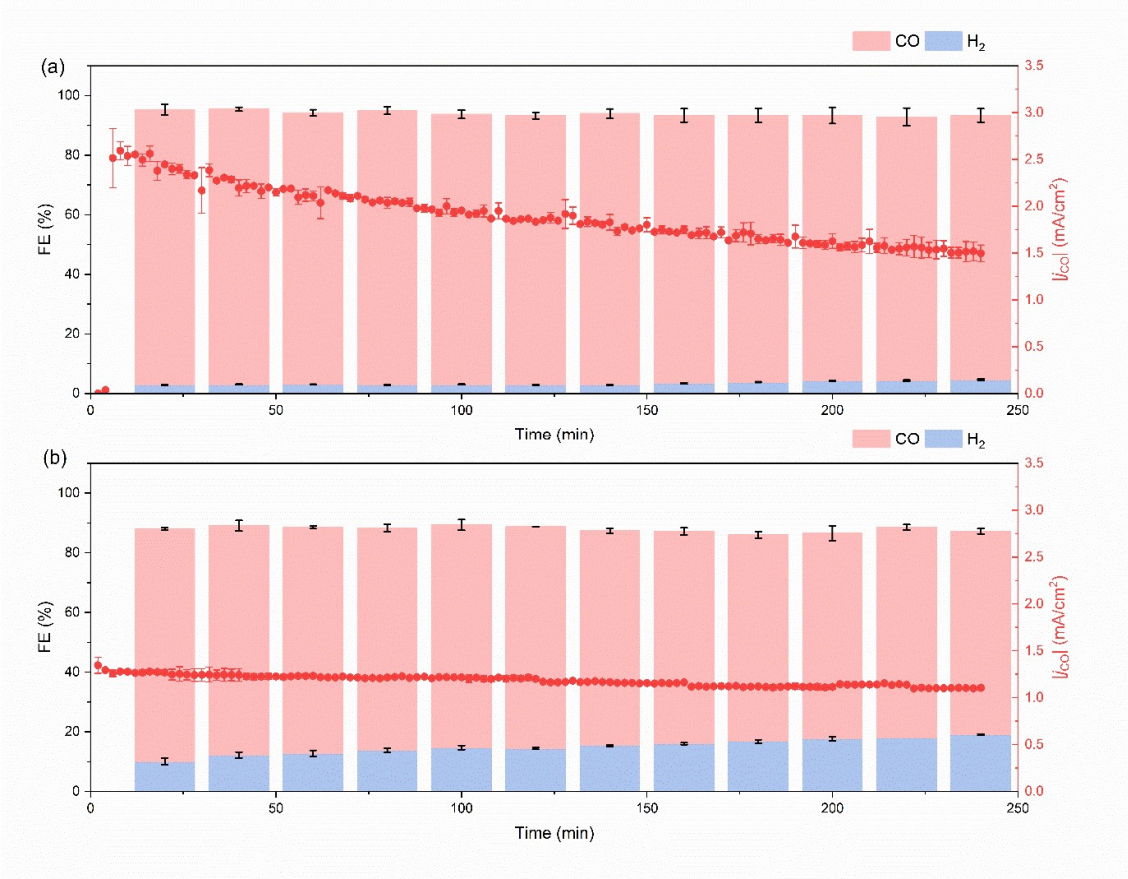

Figure S18. Faradaic efficiencies and j_{CO} during 4-hour tests for (a) ANBC and (b) Ag foil electrodes at -1.0 V vs. RHE in a CO_2 saturated 0.1 M $KHCO_3$ + 25 mM K_2SO_3 + 25 mM K_2SO_4 electrolyte.

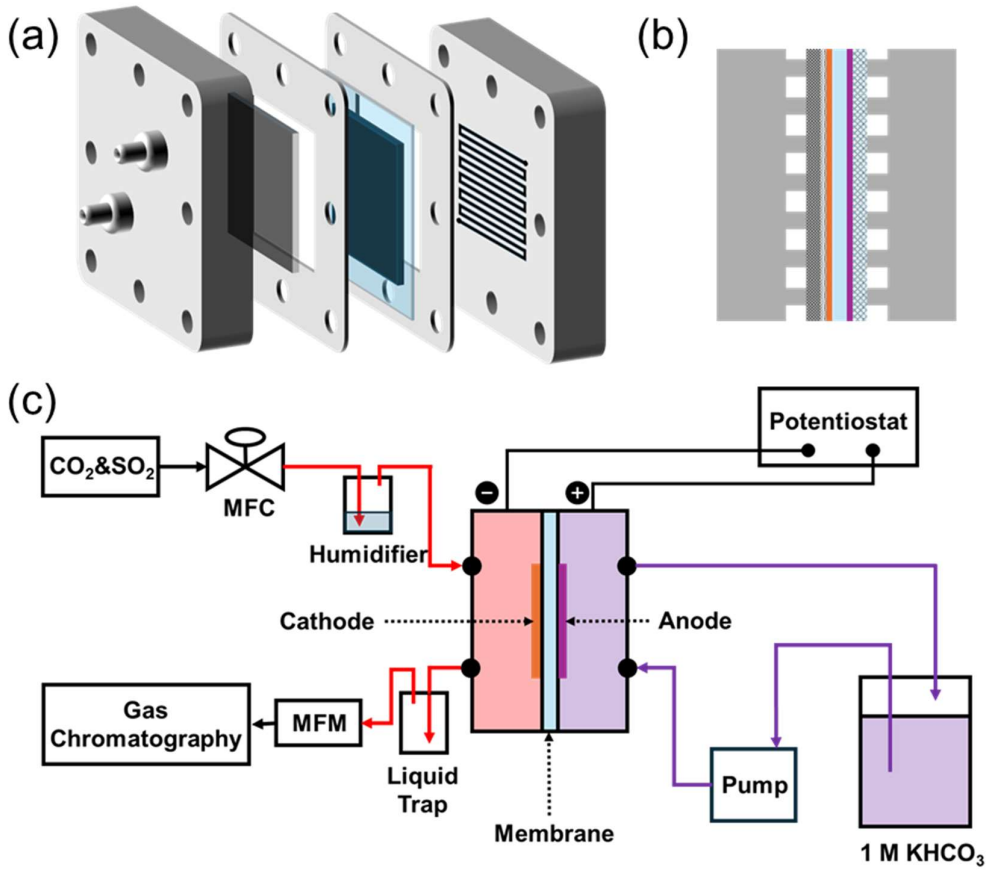

Figure S19. (a) Schematic illustration of the MEA reactor; (b) Cross-sectional view of the MEA configuration; (c) Diagram of the experimental setup for high current density CO_2 reduction measurements.

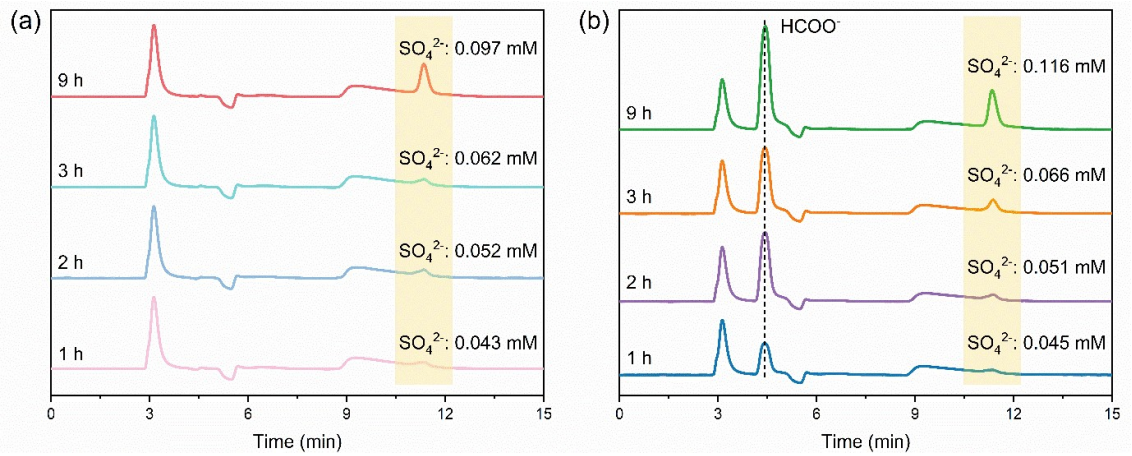

Figure S20. Ion chromatography results of post-reaction anolytes from the (a) ANBC and (b) Ag NP electrodes after CO_2RR for 1, 2, 3, and 9 hours electrolysis at 100 mA/cm^2 in the presence of 100 ppm SO_2.

Note: The IC measurements in this figure were performed using an Dionex IonPac AS22 analytical column due to replacement of the previously used Dionex IonPac AS14A column after maintenance. As a result, the chromatographic method was adjusted accordingly, leading to a longer analysis time (~15 min) compared to the previous measurements (~10 min, Figure S10). This change does not affect the qualitative or quantitative interpretation of the detected ionic species.

Table S1. Impact of SO_2 impurity on CO_2 electroreduction performance and catalyst

Feed gas	Catalyst	Reactor	Electrode area	Membrane	Electrolyte	Reaction duration with impurities	Performance	Post-reaction Catalyst	Ref.
1% SO_2 in CO_2	Ag	3-Comparment flow cell	1 cm^2	FAA-3	1 M $KHCO_3$	30 minutes	FE_{CO} decreases from 90% to 72%	Ag_2S formation on surface	18
	Sn						FE_{HCOO^-} decreases from 79% to 52%	SnS_2 formation on surface	
	Cu						FE_{C2H4} decreases from 19% to 0 % FE_{HCOO^-} increases from 13% to 35%	Cu_2S formation on surface	
0.01% SO_2 in CO_2	Ag						No significant change	-	
	Sn						No significant change	-	
	Cu						FE_{C2H4} decreases from 15% to 4%	Cu_2S formation on surface	

							FE_{HCOO^-} increases from 16% to 42%		
0.1% SO_2 in CO_2	Cu						FE_{C2H4} decreases from 17% to 0% FE_{HCOO^-} increases from 9% to 36%	Cu_2S formation on surface	
1% SO_2 in CO_2	Cu	H-Cell	2 cm^2	Nafion	0.5 M $KHCO_3$	2 hours	Total FE decreases around 16 -43%	Cu surface remains shiny	[19]
10 ppm SO_2 in a dilute CO_2 stream (50%, balanced with N_2)	Cu	MEA	1 cm^2	X37-50 Sustainion	0.1 M $KHCO_3$	2 hours	FE_{C2+} decreases from 64% to 36%	-	[20]
100 ppm SO_2 in a dilute CO_2 stream (50%, balanced with N_2)							FE_{C2+} decreases from 64% to 20%	-	

400 ppm SO_2 in a dilute CO_2 stream (50%, balanced with N_2)							FE_{C2+} decreases from 64% to 23% after 10 minutes and further decreases to 11%	Cu_2S formation on surface	
213 ppm SO_2 in CO_2	Bi_2O_3	3-Comparment flow cell	10 cm^2	Nafion 117	0.5 M $KHCO_3$ for catholyte; 1 M KOH for anolyte (Single pass)	20 hours	No significant change	-	[21]
	Ag						No significant change	-	
201 ppm SO_2 in CO_2	Cu	3-Comparment flow cell	10 cm^2	Nafion 117	0.5 M $KHCO_3$ for catholyte; 1 M KOH for anolyte (Single pass)	6 hours	FE_{C2+} decreases from 24.8% to 7% FE_{HCOO-} increases from 10.2% to ~30%	-	[22]
90 ppm SO_2 and 15% CO_2 in N_2	SnS_x	Flow cell	2 cm^2	Nafion	1 M KOH	8 hours	FE_{HCOO-} remains >70% within 8 hours	-	[23]

800 ppm SO_2 in CO_2	Sn/Cu-f	H-Cell	0.5 cm^2	Nafion 117	0.1 M $KHCO_3$	18 hours	FE_{HCOO^-} remains ~80% within 18 hours	Cu_2S formation on surface	24
	Bi/Cu-f					50 hours	FE_{HCOO^-} remains ~80% within 50 hours	-	
0.3% SO_2 and 16% CO_2 in N_2	Ni-NC	3-Comparment flow cell	1 cm^2	Nafion 117	1 M KOH	1 hour	FE_{CO} decreases from 95% to 70%	-	25
0.6% SO_2 and 16% CO_2 in N_2							FE_{CO} decreases from 89% to 30%	-	
0.9% SO_2 and 16% CO_2 in N_2							FE_{CO} decreases from 70% to 60%	-	
1.2% SO_2 and 16% CO_2 in N_2							FE_{CO} decreases from 52% to 40%	Element S formation on the surface	

Table S2. Gas mixtures for electrochemical measurements.

Gas cylinders	Gas mixtures for measurements	Total flow rate (sccm)	Recipes (sccm)		
			CO_2	CO_2 + 100 ppm SO_2	CO_2 + 10000 ppm SO_2
CO_2	CO_2	10	10	0	0
CO_2 + 100 ppm SO_2	CO_2 + 100 ppm SO_2		0	10	0
CO_2 + 10000 ppm SO_2	CO_2 + 1000 ppm SO_2		9	0	1
	CO_2 + 10000 ppm SO_2		0	0	10

Table S3. The pH values of different gas mixtures saturated electrolytes.

	CO_2	CO_2 + 100 ppm SO_2	CO_2 + 1000 ppm SO_2	CO_2 + 10000 ppm SO_2
Saturation time	15 min	15 min	15 min	15 min
Gas flow rate	10 sccm	10 sccm	10 sccm	10 sccm
pH	6.80	6.78	6.75	6.72

Table S4. Standard reduction potentials for electrochemical CO_2 reduction to CO, H_2 evolution, and SO_2 reduction reactions.

Electrochemical reduction reactions	E^o (V vs. RHE) at pH = 7
$CO_2 + 2H^+ + 2e^- \rightarrow CO + H_2O$	-0.106
$2H^+ + 2e^- \rightarrow H_2$	0
$SO_2 + 4H^+ + 4e^- \rightarrow S + 2H_2O$	0.451
$SO_2 + 6H^+ + 6e^- \rightarrow H_2S + 2H_2O$	0.347

References

(1) Frisch, M. J.; Trucks, G. W.; Schlegel, H. B.; Scuseria, G. E.; Robb, M. A.; Cheeseman, J. R.; Montgomery, J. A., Jr.; Vreven, T.; Kudin, K. N.; Burant, J. C. , et al. Gaussian09, Revision B.01. Gaussian, Inc.: Wallingford, CT, 2016.

(2) Adamo, C.; Barone, V. Toward Reliable Density Functional Methods without Adjustable Parameters: The PBE0 Model. *J. Chem. Phys.* **1999**, *110* (13), 6158–6170.

(3) Weigend, F.; Ahlrichs, R. Balanced Basis Sets of Split Valence, Triple Zeta Valence and Quadruple Zeta Valence Quality for H to Rn: Design and Assessment of Accuracy. *Phys. Chem. Chem. Phys.* **2005**, *7* (18), 3297–3305.

(4) Weigend, F. Accurate Coulomb-Fitting Basis Sets for H to Rn. *Phys. Chem. Chem. Phys.* **2006**, *8* (9), 1057–1065.

(5) He, G.; Ma, J.; He, H. Role of Carbonaceous Aerosols in Catalyzing Sulfate Formation. *ACS Catal.* **2018**, *8* (5), 3825–3832.

(6) Lu, T.; Liu, Z.; Chen, Q. Comment on "18 and 12 – Member Carbon Rings (Cyclo[n]Carbons) – A Density Functional Study." *Mater. Sci. Eng. B* **2021**, *273*, 115425.

(7) Cao, X.; Dolg, M. Segmented Contraction Scheme for Small-Core Lanthanide Pseudopotential Basis Sets. *J. Mol. Struct. THEOCHEM* **2002**, *581* (1–3), 139–147.

(8) Grimme, S.; Ehrlich, S.; Goerigk, L. Effect of the Damping Function in Dispersion Corrected Density Functional Theory. *J. Comput. Chem.* **2011**, *32* (7), 1456–1465.

(9) Lu, T.; Chen, Q. Shermo: A General Code for Calculating Molecular

Thermochemistry Properties. *Comput. Theor. Chem.* **2021**, *1200*, 113249.

(10) Grimme, S. Supramolecular Binding Thermodynamics by Dispersion-Corrected Density Functional Theory. *Chem. – A Eur. J.* **2012**, *18* (32), 9955–9964.

(11) Lu, T.; Chen, Q. Independent Gradient Model Based on Hirshfeld Partition: A New Method for Visual Study of Interactions in Chemical Systems. *J. Comput. Chem.* **2022**, *43* (8), 539–555.

(12) Lu, T.; Chen, F. Multiwfn: A Multifunctional Wavefunction Analyzer. *J. Comput. Chem.* **2012**, *33* (5), 580–592.

(13) Lu, T. A Comprehensive Electron Wavefunction Analysis Toolbox for Chemists, Multiwfn. *J. Chem. Phys.* **2024**, *161* (8), 82503.

(14) Humphrey, W.; Dalke, A.; Schulten, K. VMD: Visual Molecular Dynamics. *J. Mol. Graph.* **1996**, *14* (1), 33–38.

(15) Hansen, H. A.; Rossmeisl, J.; Nørskov, J. K. Surface Pourbaix Diagrams and Oxygen Reduction Activity of Pt, Ag and Ni(111) Surfaces Studied by DFT. *Phys. Chem. Chem. Phys.* **2008**, *10* (25), 3722–3730.

(16) Fu, S.; Li, M.; Asperti, S.; De Jong, W.; Kortlever, R. Unravelling the Effect of Activators Used in the Synthesis of Biomass-Derived Carbon Electrocatalysts on the Electrocatalytic Performance for CO_2 Reduction. *ChemSusChem* **2023**, *16(9)*, e202202188.

(17) Lobaccaro, P.; Singh, M. R.; Clark, E. L.; Kwon, Y.; Bell, A. T.; Ager, J. W. Effects of Temperature and Gas–Liquid Mass Transfer on the Operation of Small Electrochemical Cells for the Quantitative Evaluation of CO_2 Reduction

Electrocatalysts. *Phys. Chem. Chem. Phys.* **2016**, *18* (38), 26777–26785.

(18) Luc, W.; Ko, B. H.; Kattel, S.; Li, S.; Su, D.; Chen, J. G.; Jiao, F. SO_2-Induced Selectivity Change in CO_2 Electroreduction. *J. Am. Chem. Soc.* **2019**, *141*(25), 9902–9909.

(19) Zhai, Y.; Chiachiarelli, L.; Sridhar, N. Effect of Gaseous Impurities on the Electrochemical Reduction of CO_2 on Copper Electrodes . *ECS Trans.* **2009**, *19* (14), 1–13.

(20) Papangelakis, P.; Miao, R. K.; Lu, R.; Liu, H.; Wang, X.; Ozden, A.; Liu, S.; Sun, N.; O'Brien, C. P.; Hu, Y.; Shakouri, M.; Xiao, Q.; Li, M.; Khatir, B.; Huang, J. E.; Wang, Y.; Xiao, Y. C.; Li, F.; Zeraati, A. S.; Zhang, Q.; Liu, P.; Golovin, K.; Howe, J. Y.; Liang, H.; Wang, Z.; Li, J.; Sargent, E. H.; Sinton, D. Improving the SO_2 Tolerance of CO_2 Reduction Electrocatalysts Using a Polymer/Catalyst/Ionomer Heterojunction Design. *Nat. Energy* **2024**, 9, 1011–1020.

(21) Van Daele, S.; Hintjens, L.; Hoekx, S.; Bohlen, B.; Neukermans, S.; Daems, N.; Hereijgers, J.; Breugelmans, T. How Flue Gas Impurities Affect the Electrochemical Reduction of CO_2 to CO and Formate. *Appl. Catal. B Environ.* **2024**, *341*, 123345.

(22) Van Daele, S.; Cioli, G.; Choukroun, D.; Breugelmans, T. The Impact of Flue Gas Impurities on the Electrochemical Reduction of Carbon Dioxide with Copper Catalysts. *J. CO_2 Util.* **2025**, *97*, 103107.

(23) Choi, B. U.; Tan, Y. C.; Song, H.; Lee, K. B.; Oh, J. System Design Considerations for Enhancing Electroproduction of Formate from Simulated Flue Gas. *ACS Sustain. Chem. Eng.* **2021**, *9* (5), 2348–2357.

(24) Prasad, Y. S. S.; Chandiran, A. K.; Chetty, R. Bilayer Porous Electrocatalysts for Stable and Selective Electrochemical Reduction of CO_2 to Formate in the Presence of Flue Gas Containing NO and SO_2. *ACS Appl. Mater. Interfaces* **2024**, *16* (24), 31011–31022.

(25) Tian, D.; Wang, Q.; Qu, Z.; Zhang, H. J. Enabling Direct Flue Gas Electrolysis by Clarifying Impurity Gas Effects on CO_2 Electroreduction. *Nano Energy* **2025**, *134*, 110563.